Song, M., He, X., Jia, D., Xiao, R., Asgarimehr, M., Wickert, J., Wang, X., Zhang, Z. (2022): Sea Surface States Detection in Polar Regions Using Measurements of Ground-Based GNSS Interferometric Reflectometry. - IEEE Transactions on Geoscience and Remote Sensing, 60, 1-14.

https://doi.org/10.1109/TGRS.2022.3155051

Sea Surface States Detection in Polar Regions using Measurements of Ground-based GNSS Interferometric Reflectometry

Minfeng Song, Xiufeng He, Dongzhen Jia, Ruya Xiao, Milad Asgarimehr, Jens Wickert, Xiaolei Wang, Zhetao Zhang

***Abstract*—This paper analyzes the interferometric measurements of ground-based Global Navigation Satellite Systems (GNSS) stations and proposes a novel method for sea surface states detection. The novel technique benefits from a cost-effective data collection from a large number of global GNSS stations. In this study, we extend a traditional GNSS interferometry reflectometry (GNSS-IR) model so that it can be applied to a multilayer surface by considering the surface roughness, total reflectivity, and penetration loss in multilayer situations. Based on this model, the wavelet analysis is used to perform parameterization on the interferometric observations represented by the Signal to Noise Ratio (SNR). An integration factor and power curve are also proposed to characterize the surface state transition. One-year data from an Arctic geodetic GNSS station in the north of Canada are collected for analysis to validate the proposed approach with comparisons to the existing methods based on the amplitude and damping factors. The results show that the new method demonstrates good usability and sensitivity to detect surface state transitions, eg. icing, snowfall, and snow melting. However, the amplitude and damping factor-based methods derived from the single-layer model are only able to detect the pure ice surface and cannot respond to thick snow conditions. Finally, the high-resolution spaceborne images confirm the reliability of this method, exhibiting a great potential for long-term coastal sea surface detection based on the global geodetic GNSS stations and later being expected to be applied to sense cryosphere surface states.**

***Index Terms*—GNSS Interferometry Reflectometry, Sea surface detection, Area factor, Signal to Noise Ratio, Cryosphere, multilayer surface.**

I. Introduction

THE continual advancement and enhancement of the GNSS technique have enriched abundant L-band signals as remote sensing sources for the GNSS reflectometry (GNSS-R) technique. The extraction of Earth's surface parameters using GNSS reflected signals received at different platforms has gradually developed during recent decades since the first usage as a new remote sensing concept was proposed in [1][2]. Numerous studies based on the spaceborne measurements demonstrated the potential of GNSS-R to sense the Earth's surface [3], including sea surface height [4] [5][6], wind speed [7][8], soil moisture [9][10], sea ice[11][12], and potentially precipitation over calm oceans [13][14]. Compared to spaceborne scenarios, the ground-based GNSS interferometry reflectometry (GNSS-IR) technique based on interference data represented by SNR records is an even lower cost and higher temporal and spatial resolution Earth monitoring approach. This technique is a passive and multi-static remote sensing technique to obtain the Earth's surface state in nearby areas of stations. The GNSS-IR provides long-term novel information for spatial and climatic analysis in addition to traditional geodetic applications. Many previous studies have validated the availability and reliability of this approach, utilizing the geodetic antenna at no additional cost for sea level [15][16], snow depth [17][18], soil moisture [19][20], and permafrost monitoring [21].

Water environment monitoring based on a huge number of global GNSS stations offers new concepts for global water cycle monitoring [22]. The ice parameter plays an essential role in the global water cycle and climate changes, and its coverage performs a vital indicator of the global radiation budget [23]. Furthermore, unexpected ice cover changes have significant consequences for the mariculture, fishing, and transportation industries, as well as port terminals, and can result in economic and social losses [24]. At the moment, regional ice monitoring is mostly focused on dedicated observatories using microwave radar techniques with high costs. Although satellite observations have demonstrated the capability to monitor large areas [25][26], they are severely affected by weather and atmospheric factors. Observations based on optical remote sensing are unavailable when it is cloudy, and microwave monitoring can suffer from low spatial resolution [27].

Manuscript received date, 2021; revised date, 2021; accepted date. This work was supported in part by the Natural Science Foundation of China (41830110), the Fundamental Research Funds for the Central Universities (Nos. B200203110), Postgraduate Research & Practice Innovation Program of Jiangsu Province (KYCX20_0489), National Natural Science Foundation of China (42004014, 42174018), the Natural Science Foundation of Jiangsu Province (BK20200530), and the State Scholarship Fund from Chinese Scholarship Council (No. 202006710115), (*Corresponding author: Xiufeng He*)

Minfeng Song, Xiufeng He, Dongzhen Jia, Ruya Xiao, Xiaolei Wang, Zhetao Zhang are with the School of Earth Sciences and Engineering, Hohai University, 211100, No. 8 Focheng West Rd, Jiangning District, Nanjing, Jiangsu, China. Minfeng Song is also with the German Research Centre for Geosciences (GFZ), 14473 Potsdam, Germany. (e-mail: smf@hhu.edu.cn, xfhe@hhu.edu.cn, jdz@hhu.edu.cn, ruya.xiao@hhu.edu.cn, chd_wxl@qq.com)

Milad Asgarimehr is with the German Research Centre for Geosciences (GFZ), 14473 Potsdam, Germany (e-mail: milad.asgarimehr@gfz-potsdam.de).

Jens Wickert is with the German Research Centre for Geosciences (GFZ), 14473 Potsdam, Germany. Jens Wickert is also with the Institute of Geodesy and Geoinformation Science, Technische Universität Berlin, 10623 Berlin, Germany (e-mail: wickert@gfz-potsdam.de).

The GNSS-R passive remote sensing shows the potential of surface freezing states detection. The solid water surface is more conducive to reflect navigation signals and there is a large difference between the dielectric constants of solid and liquid water [28]. Based on this, we can sense the surface ice near the antenna at the station. Assuming that a large number of GNSS stations can be effectively used for surface states detection, low-cost near-coastal ice and snow monitoring with a global coverage can be achieved. Furthermore, many stations are operational for a long period and can provide new information for global climate change research and increase the added value of GNSS stations. In addition, long-term measurements also assist and validate satellite-based monitoring results especially focusing on coastal areas. Beyond the ground-based case, the sea ice detection using airborne and spaceborne GNSS-R techniques can provide excellent capabilities for sea ice change monitoring [12][29][30].

The study on ice detection using multipath interferometric signals recorded by geodetic GNSS stations is still in its initial stages. Strandberg et al. [31] modified the traditional GNSS-IR equation and proposed the relative damping factor parameter to detect the ice period of the reflected surface. That study reveals that damping factor changes are consistent with the recorded local temperature and ice observations. The residual SNR damping factor, on the other hand, is highly correlated with the roughness of the reflecting surface. However, when the surface is covered by ice and thick snow, the multilayer structure can lead to more complex changes in reflection patterns. In this case, the single-layer model fails to track the transition of surface states, especially for the thick snow layer where the signals penetrate more deeply. Furthermore, the amplitude of the residual SNR data is closely related to roughness and dielectric constant changes, implying that the damping and amplitude factors are not completely independent and uncorrelated. Therefore, the detection method based solely on the damping factor may be not optimal. Yusof et al.[32]conducted an ice thickness study based on data from GNSS equipment placed on the ice surface and used a principle similar to tide and water level monitoring to detect the height between the antenna phase center and the ice-water interface to obtain the ice thickness indirectly, with an accuracy of 7 cm. Meanwhile, it confirms the penetration of reflected GNSS signals in the multilayer surface. This ice thickness measurement method for ice identification requires more verification, but it can be combined with the ice detection method to provide more detailed information for climate research. It is worthwhile to further develop the research based on geodetic stations instead of mounting the instruments on the ice. Jacobson et al. [33] used a fitting method based on a GNSS antenna, of which the panel is placed vertically to measure the thickness of lake ice. This fitting method considers the ice dielectric parameters and the results are in good agreement with the ground-truth ice thickness, and further concluded that the ice thickness was inconsistent in different areas of the lake. This strategy of the experiment in [33] has repeatedly demonstrated sensitivity to ice thickness [34]. With a correlation coefficient of 0.7 between the monitoring findings and the actual recorded data, the same experiment of polar ice concentration monitoring using similarly positioned antennas once again confirmed the great potentials of reflected GNSS signals for ice detection [23]. Due to the specific instrument in this experiment, a worldwide monitoring is supposed to be expensive, making it difficult to popularize the method and achieve global coverage. However, sea surface states detection based on a large number of off-the-shelf GNSS stations would be an innovative and low-cost method. Furthermore, long-time series retrieval of historical data would improve the potential of historical global climate change analysis. In this paper, we present a multilayer model for the GNSS-IR technique and present detailed discussions on the power of reflection received by the geodetic antenna. Based on this multilayer model, a novel method is proposed and demonstrates a stronger sensitivity to surface state transitions.

The paper is organized as follows. The methodology is presented in Section 2. The dataset and implementation are given in Section 3 with an emphasis on the outcomes and comparisons to previous studies. Finally, concluding remarks are presented in Section 4.

II. METHODOLOGY

A. *The single-layer model for the GNSS-IR technique*

The GNSS signal reflected by the flat surface and the interference with the direct signal at low elevation angles result in a periodic oscillation of the signal SNR, which can be explained by a vector decomposition [35], as shown in Fig. 1. With different states of reflecting surfaces (water or ice), the reflected signals change in the phase and amplitude.

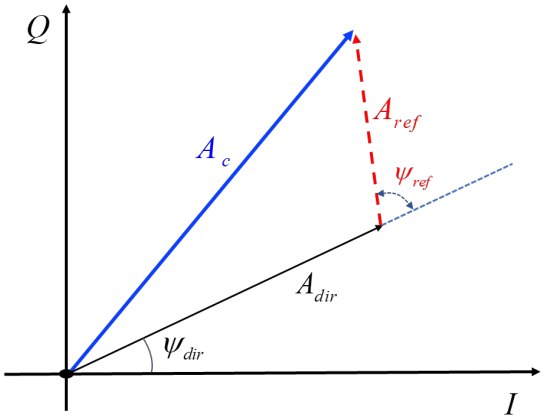

Fig. 1. Vector decomposition of interference composite signals under a single layer reflected surface conditions. I and Q refer to the in-phase and quadrature components.

In Fig. 1, $\boldsymbol{A}_c$ is the interference signal received by an upright geodetic antenna installed nearby the water surface. $\boldsymbol{A}_{\mathrm{dir}}$ is the vector of the direct signal. $\boldsymbol{A}_{\mathrm{ref}}$ is the vector of the reflected signal, containing the amplitude and phase information. ψ_{ref} is the delay phase between the direct and reflected signals, which is associated with the vertical distance h between the phase center of the antenna and the reflecting surface, i.e. $\psi_{\mathrm{ref}} = 2h\,sin(\theta)/\lambda$ [36]. λ is the wavelength of the GNSS signal. θ is the elevation angle at the geodetic antenna toward GNSS satellites. Consequently, the interference signal can be expressed by the vector of direct and reflected signal [35], as follows:

$$\begin{aligned}|\boldsymbol{A}_{\mathrm{c}}|^2 &= |\boldsymbol{A}_{\mathrm{dir}} + \boldsymbol{A}_{\mathrm{ref}}|^2 \\ &= |\boldsymbol{A}_{\mathrm{dir}}|^2 + |\boldsymbol{A}_{\mathrm{ref}}|^2 + 2|\boldsymbol{A}_{\mathrm{dir}}||\boldsymbol{A}_{\mathrm{ref}}| \\ &\quad \times \cos(\psi(\theta) + \vartheta)\end{aligned} \tag{1}$$

where $|\boldsymbol{A}_{\rm dir}|^2 = |\boldsymbol{A}_c|^2 \mathrm{F}(\theta)$. $|\boldsymbol{A}_{\rm ref}|^2 = |\boldsymbol{A}_c \Re_{ref}|^2 \mathrm{F}(-\theta)$. $\boldsymbol{A}_{\rm dir}$ and $\boldsymbol{A}_{\rm ref}$ are the direct and reflected components as shown in Fig. 1. $\Re_{ref}$ is the reflection coefficient. $|*|$ is the function obtaining the amplitude of the signal vector. $F(\theta)$ is the gain pattern of the antenna as a function of the elevation angle θ denoting the direction of incidence with respect to the horizontal plane at the phase center, and a negative sign indicates under the horizontal plane. ϑ is the random phase. As a previous analysis demonstrated, ϑ can be used to retrieve soil moisture [19]. However, changes in surface height will result in a far larger and more complex variation of delay phase compared to the random phase ϑ, so that ϑ can be ignored in this situation. Mainly, due to the directivity of antenna gain and the surface roughness loss, we have $|\boldsymbol{A}_{\rm dir}|^2 \gg |\boldsymbol{A}_{\rm ref}|^2$. Therefore, the time series of reflected signal amplitude can be obtained utilizing low-order polynomial fitting to remove the main trend domain by the direct signal, as the simplified expression (2) from Eq. (1):

$$SNR = tSNR + dSNR \tag{2}$$

where $tSNR \approx |\boldsymbol{A}_{\rm dir}|^2$ is the dominant component that refers to the direct signal's SNR data extracted from the RINEX file. $dSNR \approx 2|\boldsymbol{A}_{\rm dir}||\boldsymbol{A}_{\rm ref}| \times \cos(\psi(\theta) + \vartheta)$ represents the reflected component. $|\boldsymbol{A}_{\rm ref}|$ is affected by the gain, $F_{R/L}(-\theta)$, of the antenna with respect to the elevation angle θ, and Fresnel reflection coefficient $\Re_{R/L}$ of the RHCP (Right Hand Circular Polarization) and LHCP (Left Hand Circular Polarization) components associated with the permittivity of the reflected medium. The RHCP and LHCP components are identified by subscripts R/L. $|\boldsymbol{A}_{\rm ref}|$ can be further extended as [37]:

$$\begin{aligned} |\boldsymbol{A}_{\rm ref}| &= \left|\boldsymbol{A}_{\rm ref,R} + \boldsymbol{A}_{\rm ref,L}\right| \\ &= |\boldsymbol{A}_{\rm dir}|[\Re_R F(-\theta) + \Re_L F(-\theta)] \end{aligned} \tag{3}$$

where $\boldsymbol{A}_{\rm ref,R}$ and $\boldsymbol{A}_{\rm ref,L}$ are the RHCP and LHCP components in the reflected signals with reflection coefficients of $\Re_R$, $\Re_L$, respectively. The reflection coefficient varies with the reflected medium change and can be calculated according to the Fresnel law even in the complicated situation of multilayer, which will be analyzed later. GNSS signals are originally transmitted in RHCP, however, reaching the surface, a proportion of the signal is reflected in LHCP. The RHCP and LHCP ratio of the reflected signals is dependent on the reflection geometry. The RHCP design of geodetic antenna restrains receiving LHCP signals, which result in $\Re_L \mathrm{F}(-\theta)$ approaching zero, i.e., $\Re_L \mathrm{F}(-\theta) \approx 0$. Therefore, combining Eq.(2) and (3) and adding an attenuation item concerned to the pattern of antenna gain and roughness of the reflected surface to ensure the conformity of modeling [38], the single-layer model is built.

$$dSNR \approx \Gamma \cos(\psi(\theta) + \vartheta) \times \Upsilon(\theta, \sigma) \tag{4}$$

Where $\Gamma = 2|\boldsymbol{A}_{\rm dir}|^2 \Re_R \mathrm{F}(-\theta)$, $\Re_R$ is the reflection coefficient of RHCP signals in the single-layer reflection from layer 1 to layer 2, with relative permittivities, $\varepsilon_1 (\varepsilon_1 = \varepsilon_1' - j\varepsilon_1'')$ and ε_2 $(\varepsilon_2 = \varepsilon_2' - j\varepsilon_2'')$, respectively. $\Re_R$ can be calculated from $\Re_{12}^v$ and $\Re_{12}^h$ [39], as follows:

$$\Re_R = \frac{1}{2}(\Re_{12}^v + \Re_{12}^h), \Re_L = \frac{1}{2}(\Re_{12}^v - \Re_{12}^h) \tag{5}$$

where $\Re_L$ is the reflection coefficient of LHCP signals $\Re_{12}^v$ and $\Re_{12}^h$ are the reflection coefficients of vertical and horizontal polarization signals, respectively. $\Re_{12}^v$ and $\Re_{12}^h$ are calculated based on the Fresnel equations [39]:

$$\begin{aligned} \Re_{12}^v &= \frac{\varepsilon_1 cos\theta - \sqrt{\varepsilon_1\varepsilon_2 - (\varepsilon_1 sin\theta)^2}}{\varepsilon_1 cos\theta + \sqrt{\varepsilon_1\varepsilon_2 - (\varepsilon_1 sin\theta)^2}} \\ \Re_{12}^h &= \frac{\varepsilon_2 cos\theta - \sqrt{\varepsilon_1\varepsilon_2 - (\varepsilon_1 sin\theta)^2}}{\varepsilon_2 cos\theta + \sqrt{\varepsilon_1\varepsilon_2 - (\varepsilon_1 sin\theta)^2}} \end{aligned} \tag{6}$$

where θ is the elevation angle at the specular point. $\varepsilon_1 (\varepsilon_1 = \varepsilon_1' - j\varepsilon_1'')$ and ε_2 $(\varepsilon_2 = \varepsilon_2' - j\varepsilon_2'')$ are the relative complex permittivities of the up medium and down medium separated by a single interface.

$\Upsilon(\theta, \sigma)$ is the attenuation item that determines the declining trend of the dSNR data with the elevation angle increase. σ is the surface roughness represented by the surface height standard deviation (STD), which leads to a different variation trend in $\Gamma(|\boldsymbol{A}_{\rm ref}|)$, of the dSNR. $\Upsilon(\theta, \sigma)$ reads [31][39]

$$\Upsilon(\theta, \sigma) = \exp(-4{\psi_{\rm std}}^2) \tag{7}$$

where $\psi_{\rm std} = k\sigma \sin\theta$, λ and $\kappa = 2\pi/\lambda$ are the wavelength and wavenumber of GNSS signals. In the previous analysis, $\xi = \sigma^2$, called damping factor, is investigated by fitting approach to be as an indicator to distinguish the ice and water [31]. Consequently, the single-layer reflection model read

$$\mathrm{dSNR} \approx \Gamma(\theta) \cos(\psi(\theta) + \vartheta) \exp(-16\frac{\pi^2}{\lambda^2}\xi \sin^2\theta) \tag{8}$$

where $\Gamma(\theta)$ and ξ are called amplitude and damping factors. By analyzing and modeling the measured residual SNR data as Eq. (8), the surface information, i.e., surface height changes [40], surface roughness, and soil moisture [19] can be retrieved.

B. The single reflection over the multilayer surface

In high latitude regions, the water surface is commonly covered with ice and snow. Those changing surfaces can lead to a complicated variation in the reflection coefficient of GNSS signals. For the multilayer surface, the Multiple-Ray Single-Reflection (MRSR) model was proposed by [28] to investigate the power contribution of each reflective layer to the coherent signals based on the LHCP. Here we extend this forward model by adding the impact of the surface roughness to analyze the power of RHCP signals on each reflective layer. A simple sketch in Fig. 2 shows the reflective geometry of the MRSR model in the air-snow-ice-seawater surface.

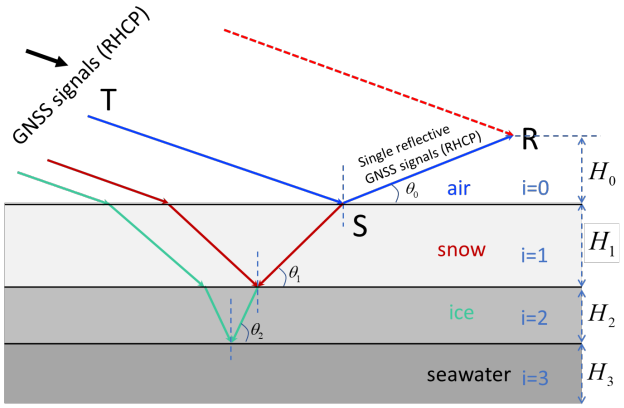

Fig. 2. The geometric path of reflection signals in the MRSR model. The seawater surface is coved by snow and ice. The RHCP signals start from the transmitter (T) and propagation to the receiver (R) after the multilayer surface reflection. The multilayer surface is composed of snow, ice, and seawater from

top to bottom, and the thickness of each layer is H_1, H_2, H_3, respectively. H_1, H_2, H_3 is the antenna height of the receiver from the snow surface. The elevation angle in the interface between H_1, H_2, H_3 and i layer is represented by θ_i.

The power of the reflected signal mainly consists of three compositions that are reflected by the three interfaces between air, snow, ice, and seawater. In general, in the air-snow-ice-seawater surface, from upper to lower levels, the permittivity increases with the penetration depth, which results in a gradually decreasing refraction angle. According to the Fresnel law, the RHCP component declines with the increment of elevation angle. Therefore, the sub-structure layers will contribute less than the first interface between air and snow.

Nevertheless, the sub-structure layer can disturb the reflection compared with the single-layer surface, especially in the low elevation angle range. Based on the MRSR model [28], the complicated composited reflected signals can be represented by a multi-vectors summation, as shown in Fig. 3.

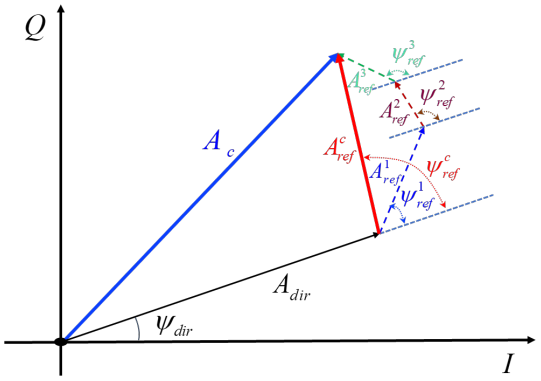

Fig. 3. Vector decomposition of interference composite signals under multi-layer reflected surface conditions.

In Fig. 3, the composite reflected signal consists of three reflective sub-signals that are reflected from different interfaces. Its amplitude and phase can be calculated by vector summations of sub-signals. Consequently, the signal received at the antenna phase center can be obtained as follows:

$$|\boldsymbol{A}_c|^2 = \left|\boldsymbol{A}_{dir} + \boldsymbol{A}_{ref}^{01} + \boldsymbol{A}_{ref}^{12} + \boldsymbol{A}_{ref}^{23}\right|^2 \quad (9)$$

where $\boldsymbol{A}_{dir}$ is the vector of direct signal, $\boldsymbol{A}_{ref}^{i-1i}$ i=1,2,3,4. are the signals reflected by the interface between $i-1$ and i layer. The direct signal can be expressed by:

$$\boldsymbol{A}_{dir} = |\boldsymbol{A}_{dir}| e^{-2\pi j k \rho_{dir}} \quad (10)$$

where ρ_{dir} is the path range of the direct signal. Each reflected sub-signal can be expressed by:

$$\boldsymbol{A}_{ref}^{i-1i} = \left|\boldsymbol{A}_{ref}^{i-1i}\right| e^{-2\pi j k(\rho_{dir}+\rho_{i-1i})} \quad (11)$$

where ρ_{i-1i} is the additional path delay of the signal reflected from the interface between $i-1$ and i layer with respect to the direct signal. $\left|\boldsymbol{A}_{ref}^{i-1i}\right|$ is the amplitude of signals reflected from the interface between $i-1$ and i layer, which is calculated as:

$$\left|\boldsymbol{A}_{ref}^{i-1i}\right|^2 = |\boldsymbol{A}_{dir}|^2 F(-\theta) U_{i-1i}^2 \Upsilon_{i-1i} \quad (12)$$

where U_{i-1i} is the total reflection coefficient of RHCP signals reflected by the interface between the $i-1$ and i layer, which reads [28]

$$U_i = R_{i-1i} \Pi_{m=1}^{m=i} T_{m-1m} T_{mm-1} e^{-2\alpha_i d_i} \quad (13)$$

where R_{i-1i}, T_{m-1m}, and θ_{i-1} are the reflection coefficient, transmission coefficient, and the elevation angle (residual angle of the incidence angle) on the interface between $i-1$ $(m-1)$ and i (m) layer. $\alpha_i = \frac{2\pi}{\lambda} |\mathrm{Im}\{\sqrt{\varepsilon_i}\}|$ is the attenuation constant [39] that attenuates the signal by combining the travel length $d_i = \frac{H_i}{\sin\theta_i}$ of signal in i layer. H_i is the thickness of i layer. ε_i is the relative complex permittivity of i layer. θ_{i-1} is calculated as:

$$\theta_i = \mathrm{acos}(\cos\theta_{i-1} \sqrt{\tfrac{\varepsilon_{i-1}}{\varepsilon_i}}) \quad (14)$$

In Eq. (12), Υ_{i-1i} is the damping item associated with the surface roughness, which can be calculated by Eq. (7) with the surface height STD, σ_{i-1i} of the interface between layer $i-1$ and i.

In Eq. (11), ρ_{i-1i} is calculated by follows[28]:

$$\rho_{i-1i} = \rho_{01} + 2\sum_{m=1}^{m=i} \frac{H_{m-1}}{\sin\theta_{m-1}} - \left(2\sum_{m=1}^{m=i} H_{m-1} \tan(90 - \theta_{m-1})\right)\cos\theta_0 \quad (15)$$

where $\rho_{01} = 2H_0 \sin\theta_0$, H_0 is the vertical distance between phase center and the first interface, H_{m-1} is the thickness of layer $m-1$. Expanding Eq. (9) and removing the main trend of the direct signal contribution in the SNR data, a simplification similar to Eq. (2) can be performed to analyze the $dSNR$ by considering: $|\boldsymbol{A}_{dir}|F(\theta_0) \gg \left|\boldsymbol{A}_{ref}^{i-1i}\right|F(-\theta_0), i = 1,2,3,4$.

$$dSNR \approx 2\sum_{i=1}^{n} \left|\boldsymbol{A}_{dir}\boldsymbol{A}_{ref}^{i-1i}\right| \cos(2\pi\rho_{i-1i}/\lambda) \quad (16)$$

where n is the number of layers of reflective surface medium, in the situation presented in Fig. 2, $n = 4$. Referring to the MRSR model and involves the influence of surface roughness, Eq. (16) can be extended as:

$$dSNR = 2F(-\theta_0)\sum_{i=1}^{n} |\boldsymbol{A}_{dir}|^2 U_{i-1i}^2 \Upsilon_{i-1i} \cos(2\pi\rho_{i-1i}/\lambda) \quad (17)$$

Eq. (17) is the multilayer model for the GNSS-IR technique associated with permittivities, layer thicknesses, surface roughness, and the elevation angle, which can be used to simulate the power of reflected signals and investigate the impact of diverse multilayer surfaces on the reflections.

C. Power analysis of the reflected signal

The influence on the power of reflected signals can be concluded into three parts. The first is the original power of the signal transmitted from GNSS satellites, which is related to the age of the GPS transmitter and its design varying in different blocks [41]. The secondary factor is the power loss due to the long-distance propagation, including the free-space propagation loss [42], and inevitable losses due to single or multiple reflections [43]. Considering the short range of elevation angle applied to the GNSS-IR technique, the free space propagation loss is neglectable, whereas the reflection loss related to the dielectric properties and roughness of the surface is regarded as the dominant [43]. The third part is the gain pattern of the antenna and the signal processing mechanism of different signals [44]. In general, the gain pattern is related to the hardware design of the antenna, and for a particular station, its impact can be weakened by differential calculations between different time epochs. It is worth noticing that the damping factor in Eq. (8) is closely related to antenna gain. Thus special attention should be paid to the gain pattern when applying quantitative geo-information retrieval based on this damping factor [38]. In summary, it can be considered that

the power of the reflected signal is mainly determined by the roughness and medium type of the reflecting surface, and both can be quantified utilizing the surface height STD and permittivity of the reflected medium. Theoretically, it is possible to detect surface states based on model parameters related to roughness and mediums.

1) Surface roughness

The waves driven by winds and swell have a direct impact on the surface roughness during the ice-free period. Generally, in an open sea area, the higher the wind speed, the rougher the surface. However, over a small inland water surface, fetches due to winds over small inland water bodies tend to be stable due to the limited fetch left for the winds to form the waves. Here we use the surface height standard deviation to qualify the surface roughness. The surface roughness model is given by Eq. (7), and the details of this can be found in [39]. Based on this model, a simulation associated with the elevation angle and surface roughness is presented in Fig. 4.

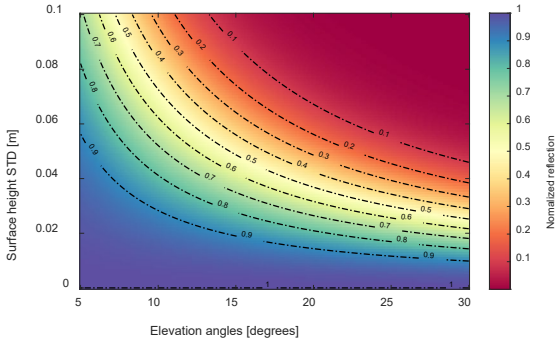

Fig. 4. Surface reflections related to surface roughness and elevation angles.

It can be seen that both elevation angles and surface roughness have an apparent impact on the signal reflection. Considering the elevation angle range from 5 to 30 degrees, the amplitude of reflection will decline faster as the elevation angle increase when the surface height STD is over 0.05m. In general, the ice surface is slightly rough compared to the water surface so that it can be distinguished by this damping information in $dSNR$ data. However, it is worth noting that smooth water surfaces at very low wind speeds can result in a comparable value of damping parameters as the ice or snow surface. In addition, both the snow accumulation and melting process can change the roughness of the reflecting surface, which is common in the high latitude regime, i.e., Arctic and Antarctica. In this complex composited state of the surface, high damping values may not be abnormal even if the surface is frozen, which means that the damping parameter-based method may not be suitable in this high latitude area.

2) Total reflectivity

The reflection coefficient is another important factor that affects the power of reflected signals, which is determined by the permittivity of the surface medium. In a single layer situation, i.e., water or pure ice, the reflection coefficient shows a similar impact on the reflection signals, resulting in a decline in reflection power with the elevation angles increase. However, in a multilayer surface, the reflection coefficient is affected by a variety of physical parameters, i.e., thickness, temperature, salinity, density, and the volumetric fraction of liquid water. In Fig. 5, we present some simulations of the total reflection coefficient concerning the thickness of different layers according to Eq. (9).

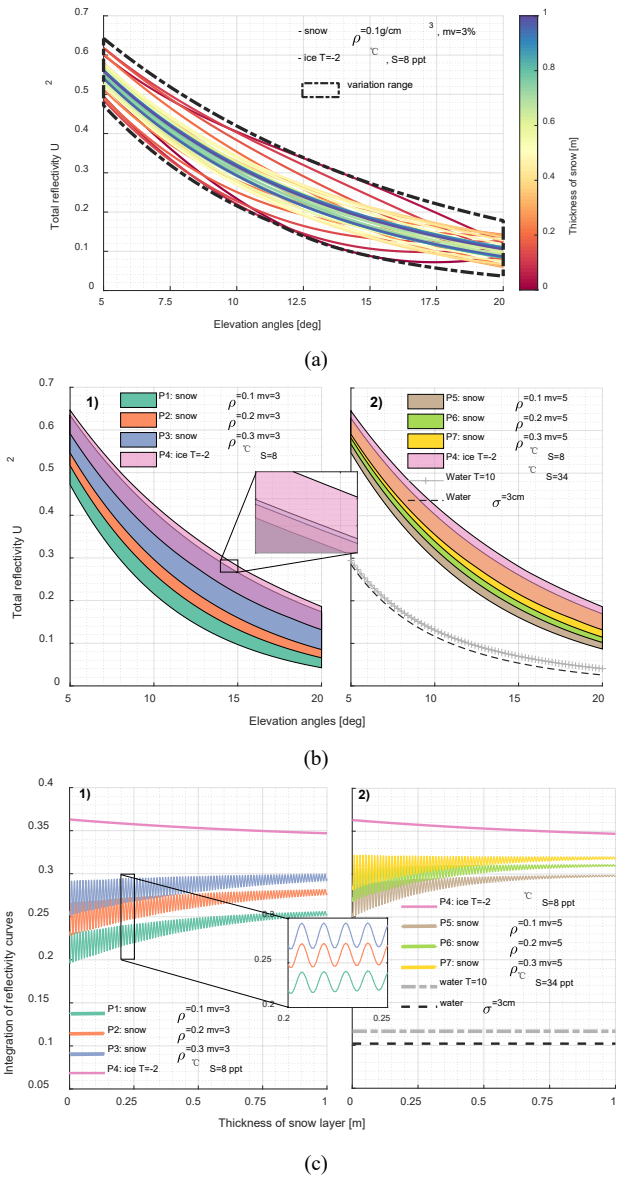

Fig. 5. Total reflectivity simulations versus elevation angles regarding the different multilayer surfaces. (a), the total reflectivity is changing within a limited range corresponding to the variations of snow and ice thicknesses from 0 to 1m. (b), the different color patches indicate the corresponding range of variations of total reflectivity due to the changes in thicknesses from 0 to 1m (snow and ice are changing independently) in different multilayer surfaces. (c) the integration of reflectivity curves in Fig. 5(b) versus the thickness of the snow layer corresponding to different surface situations with the fixed ice thickness of 0.3 m. The snow layer is mainly determined by the snow density ρ (unit: g/cm^3) and the volumetric fraction of liquid water mv (unit: %). The physical properties of ice and seawater layers are represented by temperature T (unit: degrees Celsius) and salinity S (unit: ppt). The permittivities of each layer for different physical parameters are calculated followed by the formulation in [39].

To simplify this multi-parameters simulation, firstly, the total thickness of the snow layer and ice layer is set as 1 m, which means in each simulation as the snow layer increases, the ice thickness is decreasing. A group of simulations, setting the snow density, volumetric fraction of liquid water as 0.1 g/cm^3, and 3%, temperature and salinity of ice as -2 degrees Celsius

and 8ppt, respectively, is presented in Fig. 5(a). The total reflectivity versus the elevation angle corresponding to different thicknesses of snow and ice is changing complicatedly and alternately. There is not a regular overall rising or descending trend of total reflectivity for sequence change of snow thickness but keeps a limited variation range for all the layer thickness situations. After a more comprehensive simulation with thicknesses of snow and ice layer changing from 0 to 1m independently, we found that the reflectivity is only changed in a limited range, as the dashed frame shown in Fig. 5(a). Analogously, more surface conditions related to different physical parameters are simulated, corresponding limited variation ranges are shown by the different color patches (P1, P2, P3, P4, P5, P6, P7) in Fig. 5(b), in which, the patches P1, P2, P3, P5, P6, P7 have the close up-boundary. The relative permittivities of snow, ice, and seawater are given in TABLE I.

TABLE I
PERMITTIVITIES OF DIFFERENT SURFACE LAYERS

layer	permittivity
snow	$1.54\text{-}0.052j \sim 2.24\text{-}0.11j$
ice	$3.12\text{-}0.041j$
seawater	$74.91\text{-}50.71j$

In Fig. 5(b), it can be seen that the air-snow-ice-water composited surface varying in the snow density and liquid water content will have a great impact on the total reflectivity. Different thicknesses of snow and ice will lead to the total reflectivity variations in a limited range. Comparing patches P1, P2, and P3, when the snow density increases from 0.1 $\mathrm{g/cm^3}$ to 0.3 $\mathrm{g/cm^3}$ with the same liquid water content of 3%, the reflectivity increases, and the range of variation becomes narrower and tends to be closer to the ice situation represented by the patch P4. The same results can be found when the liquid water content increases and keep the same snow density of 0.1 $\mathrm{g/cm^3}$ (Patches P1 and P5). The increases in the liquid water content result in narrowing the range of variation by raising the lower bound, which is caused by the increase in attenuation constant due to the increasing liquid water content. Accordingly, enlarging the density and the liquid water content will increase the reflectivity and reduce its range of change. In addition, the high liquid water content will increase the attenuation constant and weaken the power of reflection faster when penetrating, which is the reason why the variation range tends to be narrowed. The seawater surface maintains a stable and small total reflectivity, showing a large difference compared to the ice and snow surface, which is an apparent signature to distinguish ice and water. In addition, the impact of surface roughness involving the seawater surface demonstrates a more rapid decline in reflectivity, enlarging the difference between the water surface and other surfaces, as the comparison between the gray and black dash lines presented in the right panel of Fig. 5(b). However, it is worth noticing that the damping trend of total reflectivity in the snow surface is irregular in a wide limited range, shown in Fig. 5(a), which indicates that the damping-based method may fail to distinguish snow surface and water surface.

The snow layer is a special medium with a permittivity close to that of air, which means that L-band signals have greater penetration depth and bigger refraction angles compared to the ice layer. Therefore, stronger power of reflection from the interface between the snow and ice layer will occur a more intense interference with the reflected signal from the air-snow interference. Variations in snow thickness can lead to different degrees of interference effects between the signals reflected from the first and second interface, and demonstrate a wider range of variations.

Considering that there are overlaps in different color patches in Fig. 5(b), a further investigation on the integration of total reflectivity is carried out. In this analysis, the thickness of sea ice is fixed to 0.3m to concentrate on analyzing the impact of snow parameters. As shown in Fig. 5(c), we integrated each total reflectivity curve along with the elevation angles, and more obvious discrepancies among the different multilayer surface situations can be observed. The results demonstrate that the integration is increasing as the snow density and liquid water content increase. Despite the appearance of multiple periodic curves overlapping due to the interference effect, the magnitude relationship between these integration lines does not change, as shown in the middle zoomed-in plot. Furthermore, the water surface situations keep the lowest value and reduce with increasing surface roughness. While the ice surface maintains the largest integration of the reflectivity curve, exhibiting an apparent contrast to the other situations. These results provide us with new opportunities to detect surface states transitions.

As a result, the total reflectivities of solid water surfaces are higher than that of the water surface. Moreover, more obvious discrepancies can be observed to detect and distinguish the surface states. While the damping factor proposed in [31] will not be an optimal method to detect complex reflective surfaces with ice and thick snow layering. Therefore, based on the simulation and multilayer model, a new method of surface states detection that takes advantage of the apparent contrast between diverse states of the reflective surfaces is designed.

D. Area factor and power curve

Ice detection using amplitude and damping factors extracted from residual SNR data can be found in [31], and this study concluded that the damping factor demonstrated a better performance than the amplitude factor. However, when the surface roughness is small enough, the reflected signal power shows a declining trend similar to the first-order exponential function of height angle, while the attenuation caused by surface roughness is a second-order exponential function similar to the back trail of the normal distribution function. Accordingly, fitting the $dSNR$ data to a normal distribution function is not an optimal approach. Furthermore, the fitting model associated with the amplitude and attenuation is unstable and error-prone, especially since the $dSNR$ data have no obvious periodic characteristics. For larger attenuation rate scenarios, the amplitude factor tends to increase as the attenuation factor increases, which means that both factors are not independent. In this case, we utilize the Wavelet analysis tool to quantify the $dSNR$ data to obtain instantaneous powers of reflected signals, and then propose a new parameter to characterize surface states. Referring to the formula of energy consumption, the new factor is introduced:

$$\Theta(t) = P_{dSNR}(t) \times t \tag{18}$$

where $P_{dSNR}(t)$ is the power of the reflected signal, which is calculated via the Wavelet analysis. Θ is the Pseudo-energy, and it can be also called the area factor as it is the integral of the power curve $P_{dSNR}(t)$ along t, i.e. the area of the power curve with respect to the horizontal axis of the coordinate. $t = sin\,\theta$ is the value related to time.

Previous studies have verified the capability of the Wavelet spectrum analysis in the GNSS-IR technique to obtain instantaneous frequencies along the elevation angles [45][46]. The Wavelet transform method is based on a wavelet $\psi_w(t)$ to measure the similarity between child wavelet with scale a and translation b parameters and the input signal. The child wavelet can be defined as follows [47]:

$$\psi_w(t) = \frac{1}{\sqrt{|a|}}\psi_{a,b}(\frac{t-b}{a}) \tag{19}$$

where $a \in \mathbb{R}^+$ and $b \in \mathbb{R}$ are the scale and translation parameters, respectively. The wavelet transform is presented [46]:

$$WT_f^{\psi}(a,b) = \frac{1}{\sqrt{|a|}}\int_{\theta_{min}}^{\theta_{max}} f(sin(\theta))\psi_w^*(\frac{sin(\theta)-b}{a})\,d(sin(\theta)) \tag{20}$$

where θ_{min} and θ_{max} are the minimum and maximum elevation angles. $f(sin\,\theta)$ is the $dSNR$ data. $*$ denotes the complex conjugate. $WT_f^{\psi}(a,b)$ is the wavelet transform coefficient. The scale parameter a determines the frequency associated with the vertical height h between the antenna and reflecting surface, and the translation parameter b is related to the instantaneous elevation angle associated with time.

To facilitate subsequent calculations and ensure the consistency of the area factor obtained from each SNR segment data, the concept of full-size SNR data is introduced. The full-size SNR data means that the SNR data are continuous within the entire range of elevation angle threshold and recover both the minimum and maximum. This is a more rigorous restraint for data preprocessing compared to traditional applications but it is decent enough for surface states detection during the period of rapid development of the GNSS system.

For validation, a full-scale SNR segment data simulated by MPSIM[48] for an air-ice-seawater situation is analyzed as an instance for the explanation. A two-dimensional power spectrum as a function of the elevation angle and retrieval height RH, between the antenna and reflective surface (transformed from frequency [46]), obtained by applying the Discrete Wavelet spectrum analysis method is shown in Fig. 6.

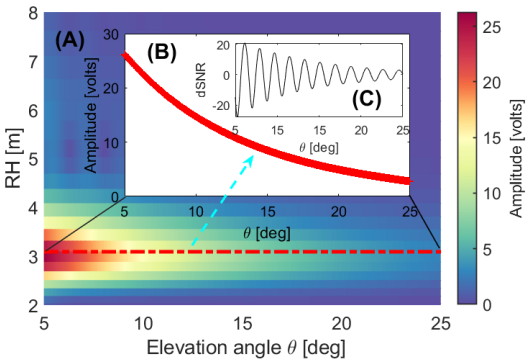

Fig. 6. The two-dimensional power spectrum(plane (A)) is obtained using Wavelet analysis on the full-scale SNR segment shown in panel(C). RH is the efficient height between the phase center of the antenna and the reflective surface, which is transformed from frequency[46]. The power curve of the $dSNR$ data extracted from the two-dimensional power spectrum is present in plane (B). The permittivities of the seawater (T=10 degrees Celsius, S=34ppt) and ice (T=-2 degrees Celsius, S=8 ppt) are: $\varepsilon_{seawater} = 74.91 - 50.71j$, $\varepsilon_{seaice} = 3.12 - 0.04j$, respectively.

In panel (B) of Fig. 6, the instantaneous power curve as a function of the elevation angle contains the amplitude and damping information of the $dSNR$ data. The amplitude and damping factors can also be obtained by fitting this power curve. Once the power curve is estimated by the Wavelet analysis, the area factor $\Theta(t, N_{\text{prn}})$ corresponding to time t and PRN (Pseudo-Random Noise) number N_{prn} of GNSS satellites can be calculated by integrating the power curve along the elevation angle:

$$\Theta(t, N_{\text{prn}}) = \frac{1}{n}\int_{\theta_{min}}^{\theta_{max}} P_{peak}^{\xi}(t, N_{\text{prn}}, \theta)d\theta \tag{21}$$

where n is the number of sampling in each $dSNR$ data. $\theta_{min}, \theta_{max}$ are the lower and upper limits of the elevation angle respectively. $P_{peak}^{\xi}(t, N_{\text{prn}}, \theta)$ is the power curve only related to reflecting surface conditions, corresponding to elevation angles, time, and PRN of GNSS satellites. $P_{peak}^{\xi}(t, N_{\text{prn}}, \theta)$ is calculated as

$$P_{peak}^{\xi}(t, N_{\text{prn}}, \theta) = P_{peak}^{o}(t, N_{\text{prn}}, \theta) - \xi_{\text{F}}(-\theta) - \delta_r \tag{22}$$

where $P_{peak}^{o}(t, N_{\text{prn}}, \theta)$ is the observed power curve estimated by the Wavelet analysis, containing damping information $\xi_{\text{F}}(-\theta)$, caused by antenna gain pattern, and random unknown errors δ_r. If the antenna gain pattern is unknown, Eq. (22) can be substituted by:

$$P_{peak}^{\xi_{\text{avg}}}(t, N_{\text{prn}}, \theta) = P_{peak}^{o}(t, N_{\text{prn}}, \theta) - \xi_{\text{avg}}(\theta, N_{\text{prn}}) - \delta_r \tag{23}$$

where $\xi_{\text{avg}}(\theta, N_{\text{prn}})$ is the average power including the damping information of antenna gain pattern and surface roughness in the ice-free surface condition. Therefore, the power curve and area factor associated with the time and the specific satellite can be obtained. In addition, the further daily area factor can be calculated by averaging the different results of all satellites.

III. Implementation and Validation Based on an Arctic Coastal GNSS Station

A. Datasets

To investigate the applicability of the new method on the condition of complex and diverse changes in the reflecting surface, we conduct a one-year experiment based on the coastal geodetic GNSS station, named TUKT. This station is located in Tuktoyaktuk, in the north of Canada, with a subarctic climate, see Fig. 7(a). Since the Arctic Ocean freezes over a long time every year, this area holds a cold winter and the temperature is much lower than normal seasons due to the minimized maritime influence. The average temperature reaches its maximum of around 10 degrees Celsius in the middle of the year. In addition, extreme cold weather dominates much time of the year resulting in less rainfall and more snowfall, with ice thicknesses up to 2 m [49] and snow depths up to 60 cm [50]. The TUKT station was installed in 2003 and equipped with an Ashtech CGRS MicroZ 12-channel dual-frequency receiver. In 2015, the receiver was replaced with Trimble NetR9. The antenna of this station is mounted on a pillar, type of ASH701945E_M, with a

height of 1.5 m over the ground, as presented in Fig. 7(b). The antenna height is about 6m from the water surface. The elevation angles range is set as 5 to 20 degrees, and the azimuth range is 8 to 125 degrees to ensure the footprint of the reflection is located on the sea surface, as the first Fresnel zone shown in Fig. 7(a). In this experiment, we collect the data from January 1 to December 31, 2018.

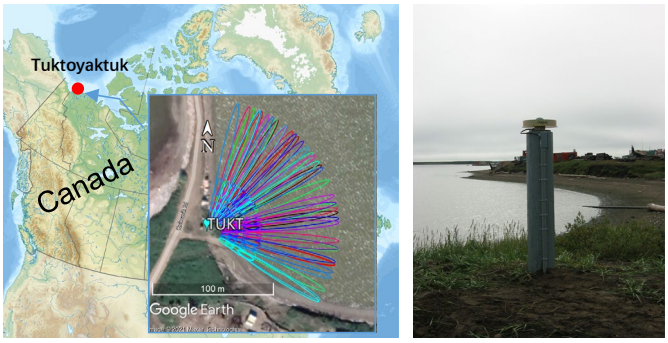

(a) (b)

Fig. 7. The location and the first Fresnel zone for elevation angles: 5, 10, 20 degrees (a) and a photograph (b) of the TUKT GNSS Station (source: https://www.sonel.org/spip.php?page=gps&idStation=864).

In addition, corresponding temperature (2 meters temperature and sea surface temperature), snow depth, snowmelt, snowfall, and snow density data from the European Centre for Medium-Range Weather Forecasts Reanalysis v5 (ERA5) are collected to verify the reliability of the results, as shown in Fig. 8.

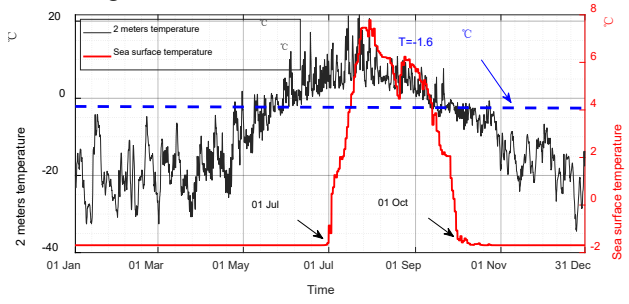

(a)

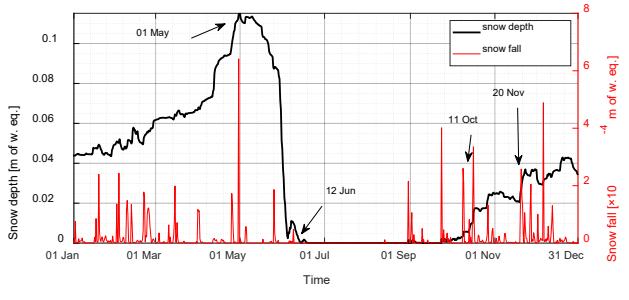

(b)

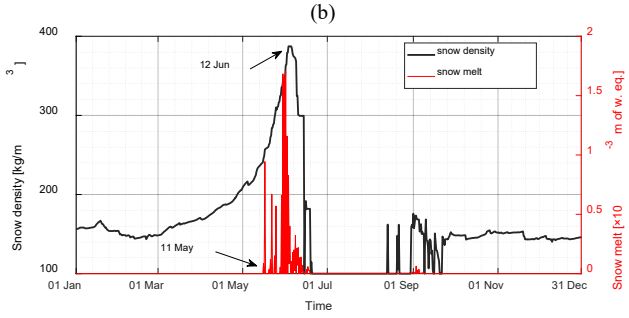

(c)

Fig. 8. The average temperature and snow-related data from the ERA5 reanalysis data at the TUTK station for the year 2018. (a) Average temperatures from the ERA5 dataset of the year 2018 at the TUKT station. The freezing point is about -1.6 degrees Celsius according to the sea surface temperature data. (b) The snow depth and snowfall data from the ERA5 dataset of the year 2018 at the TUKT station. (c) The snow density and snowmelt data from the ERA5 dataset of the year 2018 at the TUKT station. The unit [m of w. eq.] in (b-c) represents the meter of water equivalent.

In Fig. 8(a), the sea surface temperature is not synchronized with the change of the 2 meters temperature during the period of snow and ice melting. The sea surface temperature starts increasing on 30 July, while the 2 meters temperature starts to rise to -1.6 degrees Celsius on about 30 May. The melting processes of snow and ice lead to this 31-day delay, which can also be obtained in combination with Fig. 8(b) and Fig. 8(c). In addition, the surface starts freezing on 1 October, which is about 9 days after the temperature dropped to -1.6 degrees Celsius. As the temperature drops, the snow begins to accumulate immediately after the ice forms. The fresh snow keeps a low density during the beginning (1 January to 10 April) and end (1 October to 31 December) of this year. The depth of snow increases at the beginning (1 January to 10 May) and the end (1 October to 31 December) of the year, while the melting process occurs only between 10 May and 19 June.

B. Results and analysis

Based on the proposed method, one-year data of 2018 are processed and the area factor is obtained. To demonstrate more information, the image of the time series daily average power curves overlapping with the area factor results is also illustrated in Fig. 9(A). In Fig. 9(A), the area factor presents obvious variations along the time: falling, rising, and being constant, and the daily average power curves show different trends along the elevation angle. The area factor is the integral of the power curve, which reflects the overall characteristics of the reflected temporal power variation, while the power curve can exhibit more details. As shown in Fig 9(A), the area factors of 25 January and 27 October are comparable. However, the strengths of the power curves show different trends with the change of the elevation angle. The strengths of the power curve on 25 January are more concentrated at a small range of elevation angles from 7 to 9 degrees, while the strengths of the power curve on 27 October are evenly distributed in the range from 5 to 12 degrees. These differences are related to the state of the surface. As analyzed in the last section, the different states of the reflecting surfaces with diverse covered mediums, such as water, ice, snow, and their mixtures, are reflected in the power curve and area factor. Therefore, the corresponding temperature, snow depth, snowmelt, snowfall, and snow density data can be used to verify the usability and correctness of the proposed method.

The time-series results of the area factor shown in Fig. 9(A) can be separated into 3 parts. The first part is the snow accumulation period from the start of the year to 11 May and another duration from 10 October to the end of the year. In this period, the area factor decreases along the time and reaches its first local minimum point on 11 May. From the reanalysis data, we can confirm that the temperature remains almost constantly below -10 degrees Celsius, and the Tuktoyaktuk area is in a freezing period during this time. The sea surface was covered

with snow and ice between the seawater and air due to the extreme Arctic climate and long periods of intermittent snowfall. As presented in Fig. 8(b), the accumulated snow gradually reaches its highest point on 11 May. Fresh snow tends to be fluffy, and the accumulated fresh snow will increase the roughness of the interface, which is consistent with the changes in the daily power curves of this part. The strong power in the daily average power curve decays from the high elevation angles to the low elevation angles, indicating the surface tends to be rougher to decrease the coherent signals at high elevation angles. Another important fact is that the long penetration length will aggravate the attenuation of the power of the incidence signal, essentially for grazing geometric conditions. This attenuation due to the penetration loss in the reflection is holistic, therefore the area factor drops with the increasing snow depth synchronously. However, in the thick snow and melting initial period, another important point that we should notice: the ice or high-density snow loading on the antenna will reduce the power of the direct signal and lead to a decrease in the SNR data. Alternatively, the snow and ice remaining in the choke ring around the antenna may also affect the power of reflected signals, thus weakening the interference observations at low elevation angles. As shown on 05 May in Fig. 9(A), the area factor drops abruptly and then rises gradually when the temperature starts approaching the freezing point, which may be caused by the gradual melting of the snow on the antenna. The analysis above pertains to the period from 10 October to the end of the year as well. Both periods show a declined trend in area factor with the snowfall and the increase in snow depth.

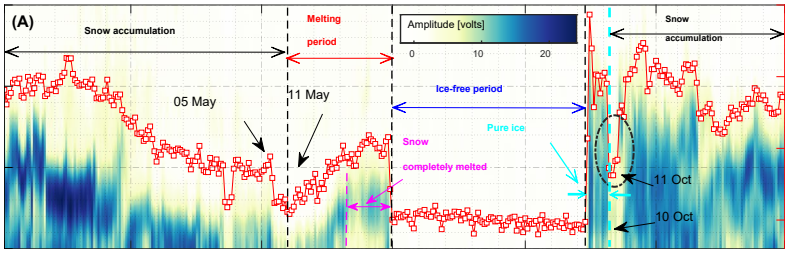

Fig. 9 (A), the area factor and the daily average power curve obtained from the S1C SNR data of the TUKT station. Based on the same data, the time-series of damping factor (B), and amplitude factor (C) were also calculated.

When the surface starts freezing, the area factor suddenly rises and reaches its highest, and then decays after the ice surface starts accumulating snow. However, around 11 October, the area factor plunges for a short time, which is caused by the abrupt accumulation of fresh snow with low density and liquid water content. As simulated in Fig. 5, fresh snow can lead to a low power curve and integration. After that, the area factor recovers to high values due to the consecutive low temperatures until another disturbance of snowfall. On 20 November, the snow depth increased suddenly according to the climatic data. Correspondingly, the area factor slightly decreases, which is consistent with the qualitative results from the simulation in Fig. 5(c). In general, the snow layer on the ice has a significant impact on the area factor. It is also due to the interference of the snow layer so that this indicator can distinguish between snow and ice.

After the first local minimum point in area factor on 11 May, the second part demonstrates a conversely temporary increase until 30 June. In this period, acknowledging from the climate information, the reflective surface undergoes complex changes due to the daily average temperature increase from -10 to 6.5 degrees Celsius. Once the temperature rises and approaches the freezing temperature (-1.6 degrees Celsius), the covered snow and ice on the reflective surface start to melt, increasing density and liquid water content, as the snowmelt data shown in Fig. 8(c). As simulated before, on the one hand, an increase in density and liquid water content can lead to a stronger reflected signal and increase the area factor. On the other hand, the high liquid water content in the snow can augment the penetration

loss. Therefore, in this period, the area factor rises gradually, but not by a large magnitude, which is consistent with the calculated area factor illustrated in Fig. 9(A). Moreover, on 12 June, the reanalysis data indicate that the snow is almost completely melted, which means that the ice is covered with a thin layer of water. In this special situation, the reflected signal is reflected by a flat and smooth layer consisting of a mixture of ice and water. As the snow gradually melts, more water will be covered on the ice surface, and the surface becomes smoother, which will shift the range location of the peak in the daily average power curve from 5 to 8 degrees for the period from 11 May to 12 June. However, in the period from 13 June to 30 June, the area factor almost keeps a sightly high value due to the ice and water mixing reflective surface with low roughness. As a result, the change of the snow state and roughness both contribute to the increase in the area factor. This part can be inferred as a melting period, in which the transitions of surface states are successfully tracked by the proposed method.

The third part from 30 June to 30 September illustrates that the area factor reaches its lowest value for a duration of 92 days due to the high temperature. In this duration, reflected signals are mainly reflected by the water surface, which is rougher compared to the ice, snow, and melting period. In addition, from Fig. 5(b), simulations demonstrate that the reflectivity of the water surface keeps a stable and lower value, and the lowest integration of the water surface can be found in Fig. 5(c). Therefore, the area factor corresponding to the water surface consistently maintains approaching zero after removing the average power curve of the ice-free period from the observed power curve. The observations shown in Fig. 9(A) during the period from 30 June to 30 September are consistent with the theoretical analysis, which confirms the sensitivity of this method for distinguishing the liquid and solid water. Another comparison between this detected ice-free date range and sea surface temperature data, showing consistency, indicates the correctness and accuracy of this new observation. Overall, the new observations obtained based on the analysis of the multilayer model response obvious variabilities on the sea surface state transitions, showing a potential opportunity for surface detection.

C. Comparison with damping and amplitude factors

To compare the proposed method with the damping factor-based method derived from the single-layer model demonstrated in [31]. This one-year data are processed using the fitting method. The $dSNR$ data are fitted as the formulation in Eq. (8) to obtain the amplitude factor and damping factor. The results are presented in Fig. 9(B-C).

In Fig. 9 (B-C), the time-series of damping and amplitude factors show a complicated trend. Firstly, it can be confirmed that both damping and amplitude factors can detect the surface transition from water to ice on 30 September, while the changes in both factors are small and not apparent compared to the sharp and sudden changes in area factor. For the inverse transition from ice to liquid water on 30 June, the damping factor fails to track the ice melting process, maintaining a value the same as the liquid water situations. As validated and analyzed before, the surface of this period (12-30 June) is a mixed surface of ice and water. Thus it can be inferred that the damping factor assumes that the surface returns to its liquid state and can not distinguish the water-ice mixture situation. Although the amplitude factor is increased compared to the ice-free period, the value corresponding to the 13-30 June period is almost the same as the initial freezing stage but involves a different surface situation. On the contrary, the area factor drops rapidly and shows a relatively small value with respect to the ice-forming period, showing a stronger sensitivity to changes in the state.

After the ice surface is gradually covered by snow starting from 1 October, the damping factor continues to maintain a low value and the amplitude factor keeps a higher value than the water surface. For the area factor, an abrupt drop occurs on 11 October, which can not be observed in the damping and amplitude factors. An empirical validation in the next part indicates that at this time point the ice surface is covered by a thick snow layer, which further proved the better performance of the new observations. With the thickness of the snow layer increasing, the changes in two factors start to become synchronized instead of the opposite. During the end period of the year 2018 from 22 November, the damping factor shows a slightly declining trend, which is opposite to the conclusion in [31]. Moreover, a more apparent weakness of the damping and amplitude factor can be observed in the first half-year. From 1 January to 12 June, the damping factor starts increasing over the value corresponding to the liquid water surface until 12 June due to the influence of the snow layer. Meanwhile, the amplitude factor demonstrates the same variation trend as the damping factor. In theory, the snow layer will increase the surface roughness and decreases the power on account of the penetration loss. However, the amplitude factor gradually raises and shows a larger value than the ice surface, which means the amplitude factor-based method is not functioning in this situation. In addition, an increase in the damping factor exceeding the abnormal indicates the invalidity of the damping factor-based method. Therefore, the results indicate that the previous method derived from a single-layer model is not suitable for a complicated multilayer surface situation.

Further investigations found that the invalidity of the previous methods is mainly caused by the fitting method based on the single-layer model inherently. The amplitude and damping factors in exponential function are not independent parameters, in which the amplitude tends to be large when the decay trend is sharp. In addition, due to the thick depth of snow on the ice, the $dSNR$ data can not be fitted effectively, which can be verified though the sparse results during 5-30 May. In the multilayer situation, the decaying impact caused by multilayer mediums is insufficient to be characterized using a single attenuation parameter. Therefore, this damping factor-based method is only suitable for the pure ice (including thin snow) and water surface.

On the contrary, the area factor shows a reasonable variation in relation to the climate data and simulation. In the duration of the thick layer of snow, reductions in the area factor due to the accumulated fresh snow with low density and water content and fresh thickness of snow layer. In summary, these two methods, although they can roughly detect the transition between water and ice, but they are not able to respond decently to the complex processes associated with the formation and melting of snow. Instead, the area factor combining the power curve shows a

strong sensitivity to sense transitions in the state of the reflective surface.

D. Validation using spaceborne images

To further confirm the usability and the correctness of the area factor, an additional investigation on relationships between specific area factors and spaceborne high-resolution images is carried out. This helps to have a better understanding of the behavior of the area factor corresponding to the surface states. The dates of selected time points are presented in Fig. 10, and their corresponding spaceborne images are shown in Figs. 11 and 12.

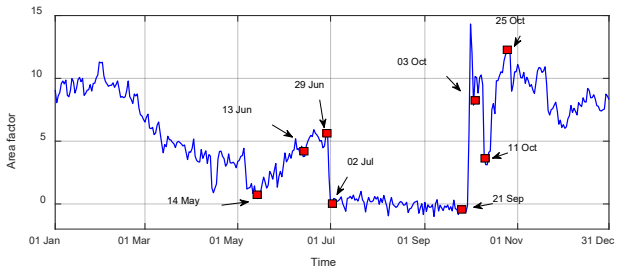

Fig. 10. The time-series of the area factor along with the dates of 8 selected points for the comparison with satellite images.

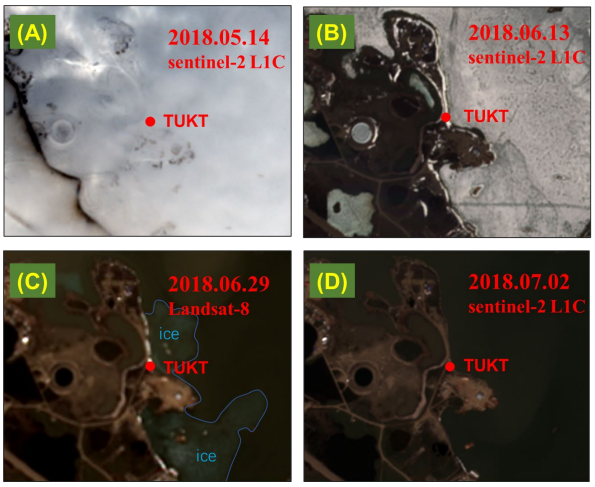

Fig. 11. The spaceborne images at the TUKT station from Sentinel-2 and Landsat-8 satellites on 2018.05.14 (A), 2018.06.13 (B), 2018.06.29 (C), and 2018.07.02 (D)

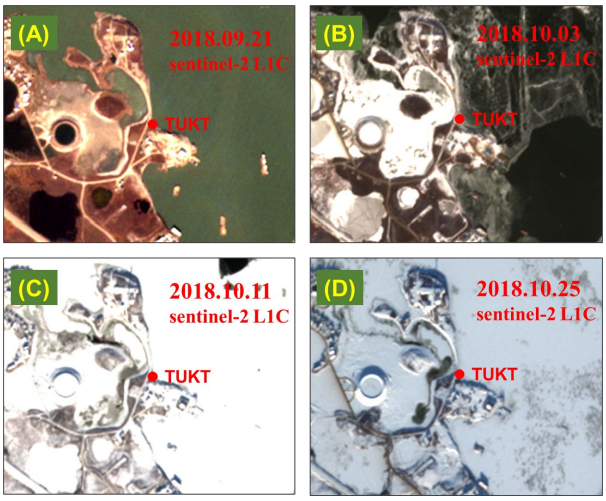

Fig. 12. The spaceborne images of the TUKT station from Sentinel-2 satellite on 2018.09.21 (A), 2018.10.03 (B), 2018.10.11 (C), and 2018.10.25 (D)

The images from the Sentinel-2 and Landsat 8 satellites provide a clear sense with a high resolution of 5m/pixels after upsampling processing. The natural color of the images can help to identify the real condition of the reflective surface. As the simulation and results discussed before, a thicker layer of snow can reduce the strength of the reflected signal. In Fig. 11(A) and Fig. 12(C), the images show that the land and ocean are covered by white snow. The coastal line near the station is even hidden in the thick snow layer in Fig. 11(A), indicating a deeper snow layer compared to Fig. 12(C). The contrast obtained from these two images is in agreement with the analysis: thick snow can lead to a low observation in the area factor. In addition, both results are larger than the pure water surface situations as shown in Fig. 12(A) and Fig. 11(D). In Fig. 11(C) and Fig. 12(B), the surfaces are covered by pure ice without snow, but both are in different stages of freezing. It can be inferred the ice shown in Fig. 11(C) is at the end of the melting stage with an additional layer of water over ice, while the other is at the beginning of ice formation. This state information is consistent with the simulation and analysis that a layer of melting water on the ice surface can reduce the reflectivity, leading to a related lower area factor of Fig. 11(C) than that of Fig. 12(B). The critical point on 29th June shown in Fig. 11 coincides well with the phenomenon at the end of ice melting shown in Fig. 12(C), which proves the correctness of this indicator.

Another special case is shown in Fig. 11(B) and Fig. 12(D). In these cases, it can be found that the ice surface tends to be gray-white, indicating that the ice surface is covered by a thin layer of snow or involves with high content of water. In addition, the snow on land in Fig. 11(B) is completely melted, which means that the reflective surface consists of water, snow, and ice, showing a good agreement with the results of the proposed method. While the thin layer of snow over ice illustrated in Fig. 12(D) is consistent with the analysis discussed before as well. Overall, changes in the state of the surface derived from the spaceborne images are consistent with the analysis based on this new observation method. Therefore, cross-validation based on high-resolution images confirms the sensitivity and correctness of the proposed method.

At the end of the cross-validation using the image data, there is one point that should be highlighted: although the high-resolution image data can be used for interpreting the state of the sea surface with wide spatial coverage to some extent, it was quite limited by the climate and extreme night in cryosphere region, resulting in sparse valid data. As we can find that the validations in Fig. 11 are mainly limited in the middle period of the whole calendar year due to the limitation of image data validity. On the contrary, the GNSS data on the ground is not affected by the climate and be collected continuously, which ensures continuity of observations. Moreover, as for the data source, the new observation is only based on the available GNSS data originally for positioning applications. Therefore the proposed method is a low-cost approach to detect more surface information, further enhancing the application value of the GNSS station.

IV. Conclusions

In this study, a new method of sea surface states detection based on ground-based interferometric observations was presented. Different from the traditional single-layer reflective surfaces, a multilayer model for the GNSS-IR technique was investigated based on the MRSR model. This method considers the surface roughness and interference influence of multi-reflections. The simulations following this multilayer model revealed the relationship between the diverse multilayer situations associated with surface medium changes and the power of reflected signals. Subsequently, two indicators, named area factor and power curve, are proposed based on the Wavelet analysis to sense the sea surface states. To validate the proposed method, one-year data from an Arctic geodetic GNSS station, located in the north of Canada, were collected for analysis. By comparing the results with the reanalysis data from ERA5, the new observations show a strong sensitivity to the surface state transitions, successfully tracking the icing, snowfall, and snow melting. However, the results of the amplitude and damping factors-based method derived from the single-layer model demonstrated a limited capacity to track the complex multilayer surface involving a thick snow layer. Finally, further validation using the spaceborne high-resolution images was carried out to verify the accuracy of this method. Comparison illustrated that proposed indicators are well consistent with the real surface information given by images, which further validated the proposed indicator for surface states detection. In summary, this method provides the potential to sense the sea surface state transition of polar regions with low-cost and long-term data, increasing the value of permanent GNSS stations. In the future, it may be expected to be further applied to ice sheet surface state monitoring in the cryosphere, combined with cryospheric GNSS stations to observe surface state data.

Acknowledgment

We appreciate Natural Resources Canada making the data of the TUKT station available to the public, and the ECWMF team for making the reanalysis data publicly available. We are also grateful to the European Commission and the European Space Agency for the Sentinel-2 and Landsat 8 datasets. Finally, we thank the anonymous reviewers for their critical reading and constructive comments on our work.

References

[1] C. D. Hall and R. A. Cordey, "Multistatic scatterometry," Remote sensing. Proc. IGARSS '88 Symp. Edinburgh, 1988. Vol. 1, pp. 561–562, 1988, doi: 10.1109/IGARSS.1988.570200.

[2] M. Martin-Neira, "A passive reflectometry and interferometry system (PARIS): application to ocean altimetry," *ESA J.*, vol. 17, no. 4, pp. 331–355, 1993.

[3] V. U. Zavorotny, S. Gleason, E. Cardellach, and A. Camps, "Tutorial on remote sensing using GNSS bistatic radar of opportunity," *IEEE Geosci. Remote Sens. Mag.*, vol. 2, no. 4, pp. 8–45, Dec. 2014, doi: 10.1109/MGRS.2014.2374220.

[4] J. Mashburn, P. Axelrad, S. T. Lowe, and K. M. Larson, "Global Ocean Altimetry with GNSS Reflections from TechDemoSat-1," *IEEE Trans. Geosci. Remote Sens.*, vol. 56, no. 7, pp. 4088–4097, Feb. 2018, doi: 10.1109/TGRS.2018.2823316.

[5] E. Cardellach *et al.*, "First Precise Spaceborne Sea Surface Altimetry with GNSS Reflected Signals," *IEEE J. Sel. Top. Appl. Earth Obs. Remote Sens.*, vol. 13, pp. 102–112, 2020, doi: 10.1109/JSTARS.2019.2952694.

[6] J. Wickert *et al.*, "GEROS-ISS: GNSS REflectometry, Radio Occultation, and Scatterometry Onboard the International Space Station," *IEEE J. Sel. Top. Appl. Earth Obs. Remote Sens.*, vol. 9, no. 10, pp. 4552–4581, 2016, doi: 10.1109/JSTARS.2016.2614428.

[7] M. Asgarimehr, J. Wickert, and S. Reich, "TDS-1 GNSS Reflectometry: Development and Validation of Forward Scattering Winds," *IEEE J. Sel. Top. Appl. Earth Obs. Remote Sens.*, vol. 11, no. 11, pp. 4534–4541, Nov. 2018, doi: 10.1109/JSTARS.2018.2873241.

[8] G. Foti *et al.*, "Spaceborne GNSS reflectometry for ocean winds: First results from the UK TechDemoSat-1 mission," *Geophys. Res. Lett.*, vol. 42, no. 13, pp. 5435–5441, Feb. 2015, doi: 10.1002/2015GL064204.

[9] M. M. Al-Khaldi, J. T. Johnson, A. J. O'Brien, A. Balenzano, and F. Mattia, "Time-Series Retrieval of Soil Moisture Using CYGNSS," *IEEE Trans. Geosci. Remote Sens.*, vol. 57, no. 7, pp. 4322–4331, Jul. 2019, doi: 10.1109/TGRS.2018.2890646.

[10] H. Kim and V. Lakshmi, "Use of Cyclone Global Navigation Satellite System (CyGNSS) Observations for Estimation of Soil Moisture," *Geophys. Res. Lett.*, vol. 45, no. 16, pp. 8272–8282, Aug. 2018, doi: 10.1029/2018GL078923.

[11] Q. Yan and W. Huang, "Sea Ice Thickness Measurement Using Spaceborne GNSS-R: First Results with TechDemoSat-1 Data," *IEEE J. Sel. Top. Appl. Earth Obs. Remote Sens.*, vol. 13, no. December 2016, p. 1, Feb. 2020, doi: 10.1109/JSTARS.2020.2966880.

[12] Y. Zhu *et al.*, "Sensing Sea Ice Based on Doppler Spread Analysis of Spaceborne GNSS-R Data," *IEEE J. Sel. Top. Appl. Earth Obs. Remote Sens.*, vol. 13, no. January 2020, pp. 217–226, 2020, doi: 10.1109/JSTARS.2019.2955175.

[13] M. Asgarimehr, V. Zavorotny, J. Wickert, and S. Reich, "Can GNSS Reflectometry Detect Precipitation Over Oceans?," *Geophys. Res. Lett.*, vol. 45, no. 22, pp. 12,512-585,592, Nov. 2018, doi: 10.1029/2018GL079708.

[14] M. Asgarimehr *et al.*, "Remote Sensing of Precipitation Using Reflected GNSS Signals: Response Analysis of Polarimetric Observations," *IEEE Trans. Geosci. Remote Sens.*, 2021, doi: 10.1109/TGRS.2021.3062492.

[15] X. Wang, X. He, and Q. Zhang, "Evaluation and combination of quad-constellation multi-GNSS multipath reflectometry applied to sea level retrieval," *Remote Sens. Environ.*, vol. 231, p. 111229, Sep. 2019, doi: 10.1016/j.rse.2019.111229.

[16] K. M. Larson, R. D. Ray, and S. D. P. P. P. Williams, "A 10-year comparison of water levels measured with a geodetic GPS receiver versus a conventional tide gauge," *J. Atmos. Ocean. Technol.*, vol. 34, no. 2, pp. 295–307, Feb. 2017, doi: 10.1175/JTECH-D-16-0101.1.

[17] K. M. Larson and E. E. Small, "Estimation of Snow Depth Using L1 GPS Signal-to-Noise Ratio Data," *IEEE J. Sel. Top. Appl. Earth Obs. Remote Sens.*, vol. 9, no. 10, pp. 4802–4808, Oct. 2016, doi: 10.1109/JSTARS.2015.2508673.

[18] K. Yu, S. Wang, Y. Li, X. Chang, and J. Li, "Snow Depth Estimation with GNSS-R Dual Receiver Observation," *Remote Sens.*, vol. 11, no. 17, 2019, doi: 10.3390/rs11172056.

[19] C. C. Chew, E. E. Small, K. M. Larson, and V. U. Zavorotny, "Effects of Near-Surface Soil Moisture on GPS SNR Data: Development of a Retrieval Algorithm for Soil Moisture," *IEEE Trans. Geosci. Remote Sens.*, vol. 52, no. 1, pp. 537–543, Feb. 2014, doi: 10.1109/TGRS.2013.2242332.

[20] F. Li, X. Peng, X. Chen, M. Liu, and L. Xu, "Analysis of key issues on GNSS-R soil moisture retrieval based on different antenna patterns," *Sensors (Switzerland)*, vol. 18, no. 8, pp. 1–16, Aug. 2018, doi: 10.3390/s18082498.

[21] Y. Hu, L. Liu, K. M. Larson, K. M. Schaefer, J. Zhang, and Y. Yao, "GPS Interferometric Reflectometry Reveals Cyclic Elevation Changes in Thaw and Freezing Seasons in a Permafrost Area (Barrow, Alaska)," *Geophys. Res. Lett.*, vol. 45, no. 11, pp. 5581–5589, Jun. 2018, doi: 10.1029/2018GL077960.

[22] K. M. Larson and E. E. Small, "Using GPS to Study the Terrestrial Water Cycle," Eos, Trans. Am. Geophys. Union, vol. 94, no. 52, pp. 505–506, 2013, doi: 10.1002/2013EO520001.

[23] A. M. Semmling *et al.*, "Sea-Ice Concentration Derived From GNSS Reflection Measurements in Fram Strait," *IEEE Trans. Geosci. Remote Sens.*, vol. 57, no. 12, pp. 10350–10361, Feb. 2019, doi: 10.1109/TGRS.2019.2933911.

[24] L. C. Brown and C. R. Duguay, "The response and role of ice cover in lake-climate interactions," *Prog. Phys. Geogr.*, vol. 34, no. 5, pp. 671–704, Jul. 2010, doi: 10.1177/0309133310375653.
[25] F. Gao, X. Wang, Y. Gao, J. Dong, and S. Wang, "Sea Ice Change Detection in SAR Images Based on Convolutional-Wavelet Neural Networks," *IEEE Geosci. Remote Sens. Lett.*, vol. 16, no. 8, pp. 1240–1244, Aug. 2019, doi: 10.1109/LGRS.2019.2895656.
[26] L. C. Brown and C. R. Duguay, "Modelling lake ice phenology with an examination of satellite-detected subgrid cell variability," *Adv. Meteorol.*, vol. 2012, 2012, doi: 10.1155/2012/529064.
[27] S. Qiu, Z. Zhu, and B. He, "Fmask 4.0: Improved cloud and cloud shadow detection in Landsats 4–8 and Sentinel-2 imagery," *Remote Sens. Environ.*, vol. 231, p. 111205, Sep. 2019, doi: 10.1016/j.rse.2019.05.024.
[28] E. Cardellach, F. Fabra, A. Rius, S. Pettinato, and S. D'Addio, "Characterization of dry-snow sub-structure using GNSS reflected signals," *Remote Sens. Environ.*, vol. 124, pp. 122–134, Feb. 2012, doi: 10.1016/j.rse.2012.05.012.
[29] E. Cardellach *et al.*, "GNSS Transpolar Earth Reflectometry exploriNg System (G-TERN): Mission Concept," *IEEE Access*, vol. 6, pp. 13980–14018, Mar. 2018, doi: 10.1109/ACCESS.2018.2814072.
[30] M. B. Rivas, J. A. Maslanik, and P. Axelrad, "Bistatic scattering of GPS signals off arctic sea ice," *IEEE Trans. Geosci. Remote Sens.*, vol. 48, no. 3 PART2, pp. 1548–1553, 2010, doi: 10.1109/TGRS.2009.2029342.
[31] J. Strandberg, T. Hobiger, and R. Haas, "Coastal Sea Ice Detection Using Ground-Based GNSS-R," *IEEE Geosci. Remote Sens. Lett.*, vol. 14, no. 9, pp. 1552–1556, Feb. 2017, doi: 10.1109/LGRS.2017.2722041.
[32] Y. Ghiasi *et al.*, "Application of GNSS interferometric reflectometry for the estimation of lake ice thickness," *Remote Sens.*, vol. 12, no. 17, p. 2721, Sep. 2020, doi: 10.3390/RS12172721.
[33] M. Jacobson, "Potential for Estimating the Thickness of Freshwater Lake Ice by GPS Interferometric Reflectometry," *J. Geogr. Geol.*, vol. 7, no. 1, pp. 10–19, 2015, doi:10.5539/jgg.v7n1p10 .
[34] J. F. Munoz-Martin *et al.*, "Snow and Ice Thickness Retrievals Using GNSS-R: Preliminary Results of the MOSAiC Experiment," *Remote Sens.*, vol. 12, no. 24, pp. 1–20, Dec. 2020, doi: 10.3390/rs12244038.
[35] A. Bilich and K. M. Larson, "Mapping the GPS multipath environment using the signal-to-noise ratio (SNR)," *Radio Sci.*, vol. 42, no. 6, pp. 1–16, 2007, doi: 10.1029/2007RS003652.
[36] M. Song, X. He, X. Wang, Y. Zhou, and X. Xu, "Study on the Quality Control for Periodogram in the Determination of Water Level Using the GNSS-IR Technique," *Sensors*, vol. 19, no. 20, p. 4524, Feb. 2019, doi: 10.3390/s19204524.
[37] A. Alonso-Arroyo, A. Camps, H. Park, D. Pascual, R. Onrubia, and F. Martín, "Retrieval of significant wave height and mean sea surface level using the GNSS-R interference pattern technique: Results from a three-month field campaign," *IEEE Trans. Geosci. Remote Sens.*, vol. 53, no. 6, pp. 3198–3209, 2015, doi: 10.1109/TGRS.2014.2371540.
[38] J. Strandberg, T. Hobiger, and R. Haas, "Improving GNSS-R sea level determination through inverse modeling of SNR data," *Radio Sci.*, vol. 51, no. 8, pp. 1286–1296, Feb. 2016, doi: 10.1002/2016RS006057.
[39] F. T. Ulaby *et al.*, *Microwave Radar and Radiometric Remote Sensing*. University of Michigan Press, 2014, ISBN-13: 9780472119356.
[40] X. Wang, X. He, R. Xiao, M. Song, and D. Jia, "Millimeter to centimeter scale precision water-level monitoring using GNSS reflectometry: Application to the South-to-North Water Diversion Project, China," *Remote Sens. Environ.*, vol. 265, p. 112645, Nov. 2021, doi: 10.1016/J.RSE.2021.112645.
[41] P. Steigenberger, S. Thoelert, and O. Montenbruck, "GNSS satellite transmit power and its impact on orbit determination," *J. Geod.*, vol. 92, no. 6, pp. 609–624, Jun. 2018, doi: 10.1007/s00190-017-1082-2.
[42] S. Jing, X. Zhan, J. Lu, S. Feng, and W. Y. Ochieng, "Characterisation of GNSS Space Service Volume," *J. Navig.*, vol. 68, no. 1, pp. 107–125, Jan. 2015, doi: 10.1017/S0373463314000472.
[43] M. Irsigler, J. A. Avila-Rodriguez, and G. W. Hein, "Criteria for GNSS Multipath Performance Assessment," Proceedings of the 18th International Technical Meeting of the Satellite Division of The Institute of Navigation (ION GNSS 2005), Long Beach, CA, September 2005, pp. 2166-2177.
[44] W. Li, E. Cardellach, F. Fabra, S. Ribo, and A. Rius, "Effects of PRN-Dependent ACF Deviations on GNSS-R Wind Speed Retrieval," *IEEE Geosci. Remote Sens. Lett.*, vol. 16, no. 3, pp. 327–331, Mar. 2019, doi: 10.1109/LGRS.2018.2875087.
[45] X. Wang, Q. Zhang, and S. Zhang, "Water levels measured with SNR using wavelet decomposition and Lomb–Scargle periodogram," *GPS Solut.*, vol. 22, no. 1, p. 22, Jan. 2018, doi: 10.1007/s10291-017-0684-8.
[46] X. Wang, Q. Zhang, and S. Zhang, "Sea level estimation from SNR data of geodetic receivers using wavelet analysis," *GPS Solut.*, vol. 23, no. 1, p. 0, Jan. 2019, doi: 10.1007/s10291-018-0798-7.
[47] F. Chen, L. Liu, and F. Guo, "Sea Surface Height Estimation with Multi-GNSS and Wavelet De-noising," *Sci. Rep.*, vol. 9, no. 1, pp. 1–10, Dec. 2019, doi: 10.1038/s41598-019-51802-9.
[48] F. G. Nievinski and K. M. Larson, "Forward modeling of GPS multipath for near-surface reflectometry and positioning applications," *GPS Solut.*, vol. 18, no. 2, pp. 309–322, 2014, doi: 10.1007/s10291-013-0331-y.
[49] A. Barker and T. Garry, "Overwintering of barges in the Beaufort - assessing ice issues and damage potential," Ottawa, Aug. 2012. Accessed: Feb. 19, 2022. [Online]. Available: https://nrc-publications.canada.ca/eng/view/object/?id=06003e42-c710-45ea-95f9-150cf0d728a7.
[50] M. J. Palmer, C. R. Burn, and S. V Kokelj, "Factors influencing permafrost temperatures across tree line in the uplands east of the Mackenzie Delta, 2004–2010," *Can. J. Earth Sci.*, vol. 49, no. 8, pp. 877–894, Mar. 2012, doi: 10.1139/e2012-002.

Minfeng Song was born in Anhui, China, in 1993. He received the B.S. degree in Changsha University of Science and Technology China, in 2017 and then he pursues his master's degree in surveying and mapping engineering from Hohai University, Nanjing, China. In 2018, he continued to pursue his Ph.D. degree through the University's Master and Doctoral Program. In 2021, he starts to study at GFZ for one and a half years. His current research focuses on Earth's surface investigation using Global Navigation Satellite System Reflectometry (GNSS-R).

Xiufeng He received the B.Eng. and M.S. degrees in control and navigation from the Nanjing University of Aeronautics and Astronautics, Nanjing, China, in 1986 and 1989, respectively, and the Ph.D. degree in navigation and survey engineering from Hong Kong Polytechnics University, Hong Kong, in 1998. In the period of 1998–1999, she was a Postdoctoral Fellow with the Norwegian University of Science and Technology, Trondheim, Norway, where she was working in guidance, navigation, and control. In 2000, she was a Research Fellow with the Global Positioning System (GPS) Center, Nanyang Technological University, Singapore. She is currently a Professor and the Director of the Institute of Satellite Navigation and Spatial Information, Hohai University, Nanjing. She has authored or coauthored three books and over 130 referred papers. Her main research interests include global navigation satellite system (GNSS), inertial navigation system (INS), GNSS reflectometry, interferometric synthetic aperture radar, and the low-cost integrated GNSS/INS navigation system.

Dongzhen Jia received the Ph.D. degree in Geodesy from Hohai University, Nanjing, China, in 2018. From 2007 to 2008, he was a Visiting Researcher with Nanyang Technological University, Singapore. He is currently a Lecturer with the School of Earth Science and Engineering, Hohai University. His research interests include GNSS data processing, deformation monitoring and 3D laser scanning applications.

Ruya Xiao received the B.Eng. degree in surveying and mapping engineering and the Ph.D. degree in Geodesy from Hohai University, Nanjing, China, in 2005 and 2015, respectively. He is currently an associate professor with the School of Earth Sciences and Engineering, Hohai University. From 2012 to 2013, he was a Research Assistant with the Institute of Space and Earth Information Science, The Chinese University of Hong Kong. From 2018 and 2020, he was a Visiting Researcher with the School of Engineering, Newcastle University, U.K. His research interest is imaging geodesy, including synthetic aperture radar interferometry (InSAR) and global navigation satellite systems (GNSS) applications.

Milad Asgarimehr received the M.Sc. degree in geodesy from the K. N. Toosi University of Technology, Tehran, Iran, in 2015, and the Ph.D. degree (Summa Cum Laude) from Technische Universität Berlin, Berlin, Germany, in 2020. Being awarded a Ph.D. Fellowship by Geo.X, the geoscientific competence network in Berlin, and Potsdam, Germany, he joined the German Research Centre for Geosciences (GFZ), Potsdam, and the Technische Universität Berlin, Berlin, in 2017. His Ph.D. dissertation was dedicated to the GNSS Reflectometry and remote sensing of the ocean and atmosphere. He is a Post-Doctoral Researcher with GFZ. His main research interests include bistatic radar, the development of novel remote sensing techniques, and studying Earth systems using the derived data especially with the help of artificial intelligence. Dr. Asgarimehr was awarded the Bernd Rendel Prize in geosciences by the German Research Foundation (DFG) in 2020.

Jens Wickert received the Diploma in physics from Technische Universität Dresden, Germany, in 1989, and the Ph.D. degree in geophysics/meteorology from Karl-Franzens University Graz, Austria, in 2002.

He was the Principal Investigator of the pioneering GPS radio occultation experiment aboard the German CHAllenging Minisatellite Payload (CHAMP) Satellite and coordinates numerous research projects on GNSS remote sensing. He holds a joint professorship of the German Research Centre for Geosciences (GFZ), Potsdam, with the Technische Universität Berlin on Global Navigation Satellite Systems (GNSSs) remote sensing, navigation, and positioning. He is also the Deputy GFZ Section Head of Space Geodetic Techniques and the GFZ Research Topic Director on "The Atmosphere in Global Change". He has authored more than 250 ISI listed publications on GNSS Earth observation.

Xiaolei Wang received her B.S. degree, Master's degree and Ph.D. drgree in the Department of Geology Engineering and Geomatics of Chang'an University, Xi'an, China, in 2013, 2015 and 2018, respectively. She is currently a lecturer at the School of Earth Science and Engineering, Hohai University. Her research interests are focused on the use of space geodetic techniques such as GNSS applied to global climate change, sea level, and earth deformation studies.

Zhetao Zhang obtained his Ph.D. with distinction from Tongji University, where his research topic was the GNSS unmodeled error. He is a researcher at the Hohai University and the Hong Kong Polytechnic University. His current research focuses on the GNSS precise positioning and navigation especially under complex conditions including canyon environment, low-cost receiver, and multi-GNSS situation, etc.